

Design of a Standard-Compliant Real-Time Neural Receiver for 5G NR

Reinhard Wiesmayr^{§,*}, Sebastian Cammerer[†], Fayçal Aït Aoudia[†], Jakob Hoydis[†]

Jakub Zakrzewski[†], and Alexander Keller[†]

[†]NVIDIA, [§]ETH Zurich, contact: scammerer@nvidia.com

Abstract—We detail the steps required to deploy a multi-user multiple-input multiple-output (MU-MIMO) neural receiver (NRX) in an actual cellular communication system. This raises several exciting research challenges, including the need for real-time inference and compatibility with the 5G NR standard. As the network configuration in a practical setup can change dynamically within milliseconds, we propose an adaptive NRX architecture capable of supporting dynamic modulation and coding scheme (MCS) configurations without the need for any re-training and without additional inference cost. We optimize the latency of the neural network (NN) architecture to achieve inference times of less than 1ms on an NVIDIA A100 GPU using the TensorRT inference library. These latency constraints effectively limit the size of the NN and we quantify the resulting signal-to-noise ratio (SNR) degradation as less than 0.7 dB when compared to a preliminary non-real-time NRX architecture. Finally, we explore the potential for site-specific adaptation of the receiver by investigating the required size of the training dataset and the number of fine-tuning iterations to optimize the NRX for specific radio environments using a ray tracing-based channel model. The resulting NRX is ready for deployment in a real-time 5G NR system and the source code including the TensorRT experiments is available online.¹

I. INTRODUCTION

Significant performance gains have been demonstrated by neural network (NN)-based signal processing for wireless communications [1]–[5]. However, little has been reported regarding the practical deployment of these algorithms in a 5G NR system. The challenges include a) real-time inference imposing strict latency constraints on the NN architecture, b) the need for a dynamic re-configuration of the modulation and coding scheme (MCS) without re-training, and c) site-specific fine-tuning to adapt the algorithms to the specific environment which even allows for continuous performance improvement after deployment.

In this work, we focus on the concept of neural receivers (NRXs) [2], [4], [6], where a single NN is trained to jointly perform channel estimation, equalization, and demapping. The concept has been first introduced in [2] with multiple-input multiple-output (MIMO) extensions in [7]. A 5G NR compliant multi-user MIMO receiver for the physical uplink

shared channel (PUSCH) is proposed in [6]. We revise our architecture from [6] and investigate two methods to support dynamic MCS configurations without the need for re-training.

Predicting the inference latency of a given neural network architecture is a challenging task for which the results strongly depend on the targeted hardware platform, the specific software stack as well as the level of code optimization. Thus, the number of floating point operations (FLOPs), weights, or layers is often used as surrogate metric to predict the model’s computational complexity. However, such metrics may lead to inaccurate conclusions due to the high level of parallelism and unknown memory bottlenecks during inference. We deploy our NRX [6] using the TensorRT inference library on the targeted NVIDIA A100 GPU platform. This ensures realistic latency measurements and allows for eliminating bottlenecks from the critical path. As a result, we propose a carefully optimized real-time version of the NRX architecture.

Another interesting aspect of machine learning (ML)-based receiver design is the inherent possibility of data-aided fine-tuning and site-specific adaptation of the algorithms. Contrary to (accidental) overfitting of the NN, the idea is to let the receiver learn the underlying channel statistics of the specific deployment scenario. Early promising results have been reported in [8] for a single user system, and recently in [9].

However, it remains a challenge to gather a sufficiently diverse real-world dataset to validate the possible gains and to quantify the required amount of training data. Some static users may produce many similar channel realizations, while a few dynamic users may generate a much richer dataset. We use ray tracing [10] to generate environment-specific channel impulse responses (CIRs) and investigate the required number of samples and training iterations for NRX fine-tuning.

Given the strict real-time constraints, we will address a similar research question as in [8] of whether a large neural network trained offline to generalize to arbitrary channel conditions performs better than a smaller, adaptive network optimized for specific scenarios. As it turns out, this principle of *generalization through adaptability* offers a competitive performance under strictly limited computational complexity and latency, though it may require additional training resources and may reduce robustness to unforeseen conditions. We like to emphasize that we do *not* assume training *on-the-fly* (i.e., online). Instead, we train periodically (or even just once) on a small dataset which can be regarded a by-product of the normal operation mode of the receiver.

*Work done during an internship at NVIDIA.

This work has received financial support from the European Union under Grant Agreement 101096379 (CENTRIC). Views and opinions expressed are however those of the author(s) only and do not necessarily reflect those of the European Union or the European Commission (granting authority). Neither the European Union nor the granting authority can be held responsible for them.

¹https://github.com/nvmlabs/neural_rx

II. BACKGROUND

We assume multi-user multiple-input multiple-output (MU-MIMO) uplink (UL) transmission from U user equipments (UEs) to a single base station (BS) with B antennas. While each UE can have multiple transmit antennas (e.g., UE u is equipped with N_u antennas), we assume that each UE only transmits a single MIMO stream.²

We consider transmission over the 5G NR PUSCH adhering to a standard-compliant orthogonal frequency division multiplexing (OFDM) frame structure with S subcarriers and $T = 14$ OFDM time symbols per slot³ and refer the interested reader to [11] for more details on 5G NR systems. With a sufficiently long cyclic prefix, the MU-MIMO input-output relation on each subcarrier $s \in \{1, \dots, S\}$ and for each OFDM time symbol $t \in \{1, \dots, T\}$ can be modeled as

$$\mathbf{y}_{s,t} = \sum_{u=1}^U \mathbf{H}_{s,t,u} \mathbf{x}_{s,t,u} + \mathbf{n}_{s,t} \quad (1)$$

where $\mathbf{y}_{s,t} \in \mathbb{C}^B$ is the received signal, $\mathbf{H}_{s,t,u} \in \mathbb{C}^{B \times N_u}$ is the MIMO channel matrix, $\mathbf{x}_{s,t,u}$ is the modulated transmit vector of UE u after beamforming, and $\mathbf{n}_{s,t} \sim \mathcal{N}\mathcal{C}(0, N_0 \mathbf{I})$ is the complex Gaussian noise with power spectral density N_0 .

While most of the resource elements (REs) (indexed by the tuple (s, t)) are allocated for data transmission, certain REs are reserved for pilot symbols (called demodulation reference signal (DMRS)) which are known to the BS and used for channel estimation. For simplicity, we will omit the indices s and t in the following.

The UEs apply codebook-based beamforming $\mathbf{x}_u = \mathbf{v}_u \tilde{x}_u$ where \mathbf{v}_u is a beamforming vector and \tilde{x}_u is the modulated transmit symbol which is taken from an 2^m -ary constellation. Throughout this paper, we focus on MCS indices i from 5G NR described in [12, Table 5.1.3.1-1], which applies QPSK, 16-QAM, and 64-QAM, with varying code rates. The m bits transmitted in \tilde{x}_u originate from random payload bits that are encoded by 5G NR compliant low-density parity-check (LDPC) channel coding and rate-matching, which depend on the MCS index i and the total number of data-carrying REs.

The goal of classical MIMO detectors as well as that of the NRX is to compute log-likelihood ratio (LLR) estimates for each of the UE's transmitted bits b from the received signal. We define the LLRs as logits, i.e.,

$$\ell = \ln \left(\frac{\Pr(b = 1 | \mathbf{y})}{\Pr(b = 0 | \mathbf{y})} \right) \quad (2)$$

and feed their estimates to the subsequent channel decoder.

A. Preliminary Neural Receiver Architecture

We briefly revisit the NRX architecture from [6] that was proposed for a single MCS and which we will extend to support varying and mixed MCS in Section III.

²In 5G NR terminology, a MIMO stream is often called *layer*.

³The preliminary NRX architecture from [6] as well as our extensions adapt to varying values of T and S without the need for retraining.

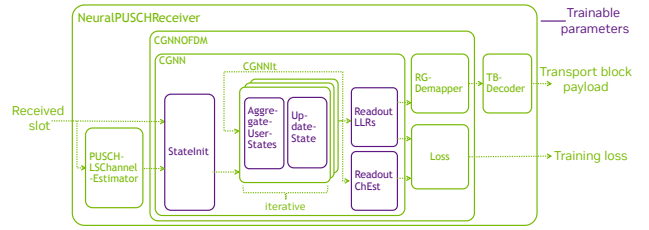


Fig. 1: Neural receiver for 5G NR PUSCH.

The NRX depicted in Fig. 1 implements a convolutional and graph neural network (CGNN) for MU-MIMO detection across the OFDM resource grid (RG). To enable 5G NR standard compliance, the CGNN is surrounded by a RG demapper and a transport block decoder (cf. Sionna's 5G NR module⁴ for details). To enable channel estimation for varying DMRS, e.g., resulting from varying slot or UE indices, a least squares (LS) channel estimator provides an initial channel estimate to the CGNN for each individual data stream.

The CGNN architecture consists of three main components: (i) the state initialization layer (`StateInit`), (ii) the unrolled iterative CGNN algorithm (`CGNNit` blocks), and (iii) the read-out layers. While the architecture in [6] only proposes one type of output layer that is used to transform the state variable to LLR estimates (`ReadoutLLRs`), our new architecture implements an additional read-out layer that outputs a (refined) channel estimate, also from the same state variable.

As detailed in [6], the `StateInit` layer implements a small convolutional neural network (CNN) that transforms the CGNN inputs, i.e., the entire RG of received signals $\mathbf{y}_{s,t}$, a positional encoding of distances to the next pilot symbol, and each UE's initial LS channel estimates, into the initial state vector $\mathbf{S}_u^{(0)} \in \mathbb{R}^{S \times T \times d_s}$ of depth d_s . The main part of the NRX consists of an unrolled iterative algorithm that applies N_{it} consecutive `CGNNit` blocks, each of which updates the state vectors of all UEs in parallel. Each `CGNNit` block first performs a message passing step where a multilayer perceptron (MLP) is used to transform each UE's state to messages, which are then aggregated by taking for each UE the sum of messages from all other UEs. The second part of each `CGNNit` block is composed of a CNN that updates each UE's state based on the previous iteration's state, the aggregated message-passing messages, and the positional encoding. After N_{it} such `CGNNit` blocks, readout MLPs are applied to transform the final state vectors $\mathbf{S}_u^{(N_{it})}$ into the desired outputs. As in [6], the `ReadoutLLRs` layer outputs LLR estimates $\hat{\ell}_{s,t,u} \in \mathbb{R}^m$ for each UE's symbol of all REs on the RG.

We extend the NRX from [6] by an additional read-out layer, denoted as `ReadoutChEst`, that outputs refined channel estimates computed from the same state vectors $\mathbf{S}_u^{(N_{it})}$. This `ReadoutChEst` layer not only provides more accurate channel estimates, it is also found to improve the training convergence when applied using an additional mean squared error (MSE) loss term as described in the following.

⁴<https://nvlabs.github.io/sionna/api/nr.html>

B. Training Scheme of the Neural Receiver

The NRX from [6] is trained by empirical risk minimization with the binary cross-entropy (BCE) loss that is computed between the LLR estimates and ground-truth bit labels. A training step describes one gradient-based weight update that is computed from the average loss of N independent samples. Each of these N batch samples represents transmission of one entire OFDM RG. If not stated otherwise, the NRX is trained on synthetic training data sampled from the 3GPP urban microcell (UMi) channel model. For each batch, the number of active users $1 \leq U_A \leq U$ is randomly sampled from a triangular distribution [13], and, in each batch sample, each UE transmits random payload bits that are individually encoded and modulated. The signal-to-noise ratio (SNR) is random-uniformly sampled (in the log-scale) for each batch sample from a pre-defined SNR range, which is a hyperparameter.

We propose the following extensions to the training scheme from [6] and detail additional considerations for variable-MCS NRX (Var-MCS NRX) in Section III-A.

1) *Double-readout*: The `ReadoutChEst` layer can be jointly trained with the `ReadoutLLRs` layer by adding an MSE loss to the BCE loss. The MSE loss is computed between the output channel estimates and the ground-truth channel realizations, and scaled by a hyperparameter γ that controls its contribution to the total loss (i.e., the sum of BCE and scaled MSE loss) used for gradient computation.

2) *Multi-loss*: To support a variable number of unrolled NRX iterations $1 \leq N'_{it} \leq N_{it}$, the NRX is trained with the so-called multi-loss [14]. There, the read-out layers are applied to the state variable after each NRX iteration and the total loss is accumulated from the loss of all N'_{it} model readouts.

III. NEURAL RECEIVERS WITH VARIABLE MCS

In this paper, we study two approaches to extend the NRX architecture from [6] to support variable modulation schemes⁵: (i) *masking* of higher-order LLRs, and (ii) *MCS-specific input and output layers* (abbreviated by *Var-IO*).

The first method builds upon an idea mentioned in [2], which was later implemented for a neural demapper in [15]. The working principle builds upon the recursive structure of bit labels from Gray-code-labeled QAM constellations, where constellation points from higher-order modulations are recursively derived from lower-order points. The higher-order bit labels then re-apply the lower-order bit labels, and are extended by the additional higher-order bits. For example, if we compare 16-QAM to QPSK, all 16-QAM constellation points within a quadrant of the complex plane have lower-order bits identical to the corresponding QPSK constellation point. Thus, by masking of unused higher-order LLR outputs, an NRX for the highest modulation order can be applied for detecting lower-order constellation points, too. As mentioned in Section III-A, training such a Var-MCS NRX requires additional considerations.

⁵The code rate and coding scheme is transparent to the NRX, as the NRX outputs LLRs on coded bits.

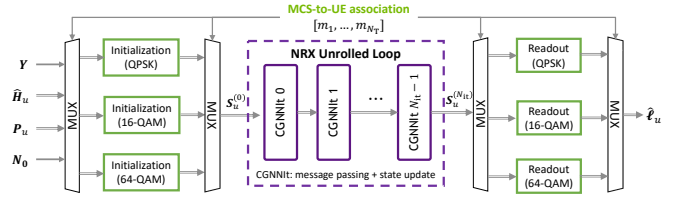


Fig. 2: Var-MCS NRX architecture with Var-IO layers.

Note that masking can be also applied to classical LLR demapping algorithms, e.g., to a posterior probability (APP) demapping. Though such *mismatched demapping* will produce LLRs with the same sign as a *matched demapper* for the correct constellation, the LLR magnitudes do in general not match the underlying probabilities, as defined in (2). Without additional LLR correction, such as proposed in [16], “classical” mismatched demapping can lead to severe performance degradation in forward error correction (FEC) decoding.

While our proposed training scheme discussed in Section III-A turned out effective to train a Var-MCS NRX with the masking scheme [15] for Gray-code labeled QAM constellations, we also put forward an alternative method for implementing the Var-MCS NRX. By applying modulation-specific `StateInit` and `ReadoutLLRs` layers (denoted as input and output layers, respectively), we allow the NRX to fit to varying modulation orders, while sharing the majority of weights (in the `CGNN` blocks) across modulation schemes. Modulation-specific input layers are motivated by improving data-aided channel estimation. The intuition for modulation-specific output layers is to enable the model to learn *matched* demapping. Only the number of LLR outputs needed for the corresponding modulation order has to be implemented. This Var-IO scheme (as depicted in Fig. 2) can be also useful with more general, non-Gray-code-labeled constellations, or custom constellations obtained from end-to-end learning [1]. Note that although MCS-specific IO layers lead to a slightly increased number of weights, the number of active weights (and, thus, the inference latency) is the same as for the single-MCS NRX.

A. Training with Mixed Modulation and Coding Schemes

It has been empirically observed that training a Var-MCS NRX requires additional considerations beyond those mentioned in Section II-B, which we detail in the following:

1) *Random MCS-to-UE association*: For each training sample and each UE, we sample an independent and identically distributed (iid) random MCS index from a set of supported MCS. This ensures that both, single-MCS and mixed-MCS transmission scenarios, are represented in each training batch. Note that explicitly training for all possible MCS-to-UE associations is infeasible due to the large number of different transmission scenarios. E.g., for eight active UEs and four MCSs, we find 165 *different* associations even without considering the order or cases where not all UEs are active.

2) *MCS specific SNR offsets*: As higher MCS and a larger number of active users typically result in higher error-rates and higher training loss for a given noise variance N_0 , we apply offsets to the random training SNR (in decibels) of

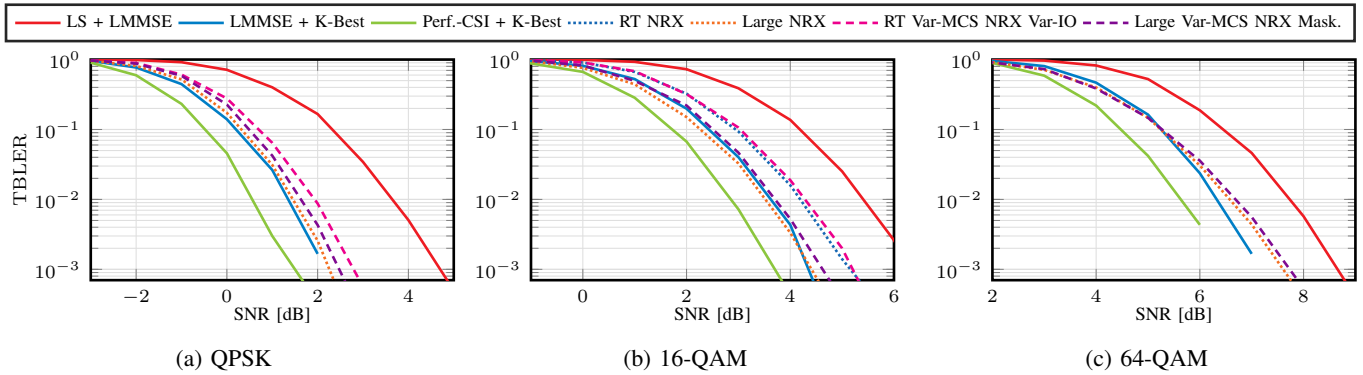


Fig. 3: Transport block error rate (TBLER) vs. SNR for a Double-TDL channel with $U \times B \equiv 2 \times 4$. The MCS indices are $i = 9$ (left), $i = 14$ (middle) and $i = 19$ (right). Dotted curves denote single-MCS NRXs and the Var-MCS NRXs are dashed.

each batch sample depending on the random number of active UEs and depending on the random MCS-to-UE association. This ensures that batch samples with higher MCS indices are trained (on average) on larger SNR values than batch samples with lower MCS indices. Thereby, we can avoid that the batch loss is dominated by batch samples with many high-MCS UEs.

B. Simulation Results

We now evaluate the TBLER performance of the Var-MCS NRX in a MU-MIMO scenario with $U = 2$ UEs transmitting in UL direction to a BS with $B = 4$ antennas. The BS has dual-polarized antennas with 3GPP TR 38.901 antenna patterns, arranged in a horizontal uniform linear array (ULA). The UEs implement two single-polarized omnidirectional antennas which are also arranged in a horizontal ULA, and apply beamforming with $\mathbf{v} = [1, 1]^T / \sqrt{2}$. In this section, we adopt the 3GPP UMi channel model for training. For evaluation, we combine two tapped delay line (TDL) models, namely 3GPP TDL-B with 400 Hz Doppler spread and 100 ns delay spread for the first user and 3GPP TDL-C with 100 Hz Doppler spread and 300 ns delay spread for the second user, respectively. In the following, we denote the resulting TDL channel model as *DoubleTDL* channel. We simulate 5G NR compliant OFDM slots with a carrier frequency of 2.14 GHz and a bandwidth of approximately 47.5 MHz, which equals 132 physical resource blocks (PRBs), each of which consists of 12 subcarriers spaced with 30 kHz. For the pilots, we select *DMRS type A* with one additional DMRS position.

We compare two different NRX architectures both with a feature depth of $d_S = 56$. We denote the first architecture as *Large NRX* which consist of $N_{it} = 8$ CGNN iterations and a total of $4.4 \cdot 10^5$ weights. A reduced architecture is denoted as *Real-time (RT) NRX* and consists of only $N_{it} = 2$ CGNN iterations resulting in only $1.4 \cdot 10^5$ weights. The Var-MCS NRX stores $0.4 \cdot 10^5$ additional weights per set of IO layers.

Fig. 3 compares the TBLER performance of various NRXs and classical baselines. The RT Var-MCS NRX is trained by randomly sampling iid uniformly from MCS index $i = 9$ (QPSK) and $i = 14$ (16-QAM), and the Large Var-MCS NRX is trained by additionally sampling iid uniformly from

$i = 19$ (64-QAM).⁶ Note that the selection of $i \in \{9, 14, 19\}$ covers *all* modulation orders defined in [12, Table 5.1.3.1-1]. The results in Fig. 3 show that all NRX architectures are capable of approaching the performance of the linear minimum mean square error (LMMSE) channel estimation baseline with K-Best detection.⁷ In all scenarios, the Var-MCS NRXs implementations closely approach the performance of their single-MCS NRX counterparts.

IV. NRX COMPLEXITY AND REAL-TIME ARCHITECTURE

Practical deployment of the NRX requires real-time inference capabilities, which imposes strict constraints on the computational latency of the underlying NN architecture. Further, the real-time aspects prevent from processing multiple samples in parallel (*inter-frame* parallelization) and only *intra-frame* parallelization can be utilized as buffering would be required otherwise. We assume a strict computational latency budget of 1 ms for the NRX using an NVIDIA A100 GPU. Furthermore, we assume inline acceleration, i.e., we ignore any *memcpy* latencies from host to device and vice versa.

A. Latency Measurements & Optimization

As mentioned earlier, it is a non-trivial task to predict the inference latency only from the model description. This stems from the fact that during inference many processing steps happen in parallel and also the memory access can become the bottleneck. To get a more realistic latency measure, we deploy the trained NRX model using TensorRT as real-time inference engine. The resulting TensorRT engine applies advanced optimization techniques tailored to the targeted inference hardware (and software stack) such as the fusing of operations during model inference. This process resembles the compilation of source code to a target deployment platform.

Weights are quantized to *float16*. However, we did not implement quantization-aware training techniques in the scope of this work. Exploring even lower quantization levels such as *float8* or *int8* precision is a subject of future research.

⁶For 64-QAM, we observed a larger performance gap between the RT and the Large NRX architecture as compared to QPSK and 16-QAM. Hence, we consider the RT NRX architecture only for detecting QPSK and 16-QAM.

⁷Covariance matrices for LMMSE channel estimation are computed from the 3GPP UMi model and the K-Best detector applies a list size of $k = 64$.

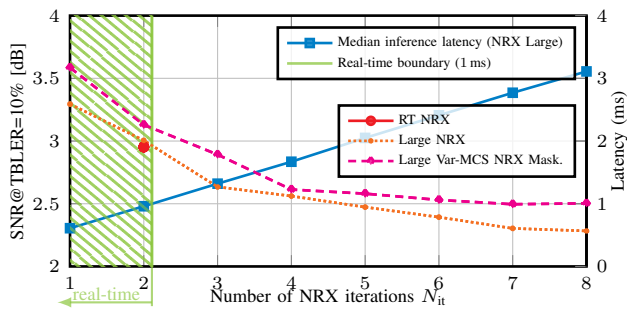


Fig. 4: SNR performance vs. number of NRX iterations for $U \times B \equiv 2 \times 4$ MU-MIMO, Double-TDL channels and 16-QAM. NRX inference latency measured on NVIDIA A100.

Based on the detailed profiling output of the TensorRT deployment, we carefully adjust the TensorFlow model. Removing compute (and memory) bottlenecks is a cumbersome task that requires carefully performed optimization steps. For brevity, the details are omitted here (though the optimized architecture is available in the code release). We like to emphasize that even if a bottleneck is identified, removing the operation may not solve the problem, as one also needs to understand its impact on the SNR performance of the NRX.

B. Controlling the Inference Latency

As mentioned in Sec. II-B, we incorporate a multi-loss [14] in the NRX training pipeline which enables to adjusting the depth of the NRX during inference without the need for any re-training. Thereby, we can control the receiver’s computational latency and the accuracy of the NN after training, e.g. to adapt to new hardware platforms or varying system configurations.

Fig. 4 shows the required SNR to achieve a target TBLE of 10% evaluated for different receiver depths $N_{it} \in \{1, \dots, 8\}$. The Large NRX is trained only once for $N_{it} = 8$ CGNN iterations (using multi-loss). The second axis in Fig. 4 shows the corresponding latency in milliseconds evaluated on an NVIDIA A100 GPU. The latency of the NRX is measured using the exported TensorRT engine and increases linearly with the number of iterations. This is to be expected, as each iteration has the same cost. For the given system configuration of 132 PRBs and 2 active UEs, each iteration requires approximately $350 \mu\text{s}$ and we observe a constant initialization (and readout) overhead of $270 \mu\text{s}$.

As can be seen in Fig. 4, the strict computational latency constraint of 1 ms restricts the receiver to $N_{it} = 2$. For comparison, we also evaluate another NRX architecture that was trained for 2 iterations only (*RT NRX*). The performance degradation of the adaptive receiver version is almost negligible. From the TBLE curves, it follows that $N_{it} = 2$ is a sub-optimal solution for the achievable error-rate performance. This implies that in a practical deployment scenario, the achievable TBLE performance of the proposed NRX is limited by its inference latency (and computational complexity).

The proposed real-time NRX architecture is applicable for practical deployment and achieves a strong performance when compared to classical baselines. However, the remaining gap

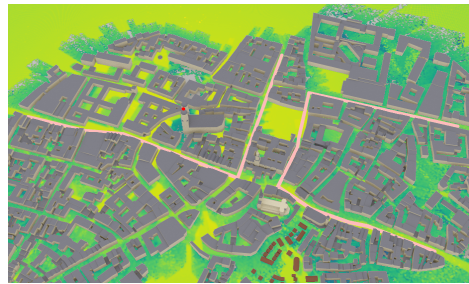


Fig. 5: Ray tracing environment using Sionna’s Munich map, augmented with coverage map, visualizing BS as red point, and UE evaluation trajectories as salmon-colored lines.

to the larger NRX shows that there is still some potential for future work. Finally, we want to underline that these experiments including the training results are available online.¹

V. SITE-SPECIFIC FINE-TUNING

In this section, we investigate how well a generalized NRX performs after site-specific deployment in a specific radio environment. Furthermore, we want to answer how much training data is needed for site-specific fine-tuning and how many fine-tuning training steps are required to improve the performance over the pre-trained generalized NRX.

A. Ray Tracing-based Training and Evaluation Dataset

We deploy the BS antenna array in Sionna’s ray tracer [10] in the Munich map on top of a church tower of the Frauenkirche, as depicted by the red dot in Fig. 5. We equip the BS and UEs with the same antenna configurations as in the experiments in Section IV. However, as the BS should cover the whole area all around the church tower, we apply isotropic antenna characteristics instead of the 3GPP TR 38.901 antenna pattern used for NRX pre-training.

For generating the training dataset, we randomly sample positions from the coverage map and compare different numbers of training data samples N_{TD} . We only add data samples that have at least one valid path between any transmit and receive antenna, for all of the $T = 14$ OFDM symbols. Together with each random position, we also sample random UE velocities uniformly in $[0, 8]$ m/s, independently for both, the x- and y-velocity, which induces a Doppler shift to the CIR.

The evaluation dataset is generated from two trajectories (one for each UE, depicted by the salmon-colored lines in Fig. 5), whereof we sample 10^4 positions uniformly between the starting and end points. Each of the two UEs moves at a constant speed, 3.5 m/s and 3.0 m/s, respectively. Sample indices where the ray-tracer did not find any valid path for either of the two UEs are removed. During simulation, we construct MU-MIMO channels by randomly sampling *two different* indices in $\{1, \dots, 10^4\}$ for each batch sample, which selects one position for each UE from their respective trajectory (random sub-sampling).

B. Effect of dataset Size and Fine-tuning Training Iterations

We now compare the effect of the training dataset size N_{TD} and the number of fine-tuning training iterations N_{FT} .

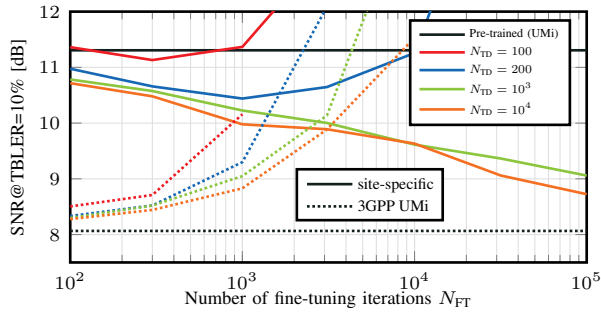


Fig. 6: SNR performance of RT NRX with fine-tuned weights for varying N_{FT} and N_{TD} in $U \times B \equiv 2 \times 4$ MU-MIMO with MCS index $i = 14$. Solid curves benchmarked on site-specific evaluation dataset, dashed curves on 3GPP UMi channels.

For fine-tuning training, we start with the NRX weights from Section IV that have been extensively pre-trained on the 3GPP UMi channel model. Then, we apply N_{FT} gradient-descent steps with the site-specific training data. Since ground-truth channel state information (CSI) data is typically not available in real-world datasets, we fine-tune without double-readout.

In Fig. 6, we visualize the performance gains achieved with site-specific training. On the y-axis we compare the required SNR to achieve a TBLE of 10% for different training dataset sizes N_{TD} . The solid curves are evaluated on the ray tracing-based evaluation dataset. We can see that very small datasets (with $N_{TD} \in \{100, 200\}$) only lead to improvements in the early fine-tuning iterations, but show degraded performance for $N_{FT} > 10^3$. With the two larger datasets ($N_{TD} \in \{10^3, 10^4\}$), the SNR performance of the NRX increases up to $N_{FT} = 10^5$. We expect this phenomena to be caused by overfitting of the NRX to the small datasets. Note that $N_{FT} = 10^3$ fine-tuning steps only take about 30 s on an NVIDIA RTX 3090 GPU.

The dotted curves in Fig. 6 visualize the SNR performance of the site-specific NRX weights evaluated on the 3GPP UMi channel model. These curves show the effect of *catastrophic forgetting*, as we see degraded performance on UMi channels, the better the NRX is fine-tuned to the ray tracing-based radio environment. Catastrophic forgetting happens more with smaller training datasets, where the effect of overfitting is more dominant. Note that more advanced training schemes based on concepts of *transfer learning* may help to further improve the training convergence and to reduce the effect of catastrophic forgetting. See [8] for an early investigation.

In Fig. 7, we evaluate the TBLE of the NRX and other *classical* baselines using site-specific data. We observe that the fine-tuned RT NRX with $N_{FT} = 10^5$ closely approaches the performance of the Large NRX without fine-tuning. The fine-tuned Large NRX with $N_{FT} = 10^3$ closely approaches the K-Best baseline with LMMSE channel estimation.

VI. CONCLUSION

We have proposed solutions for deploying of NRXs in real-world 5G NR systems: (i) adaptability for operation with variable and mixed MCS conditions, (ii) a real-time architecture that meets the latency requirements of practical software-defined 5G NR systems, and (iii) generalized NRX pre-training

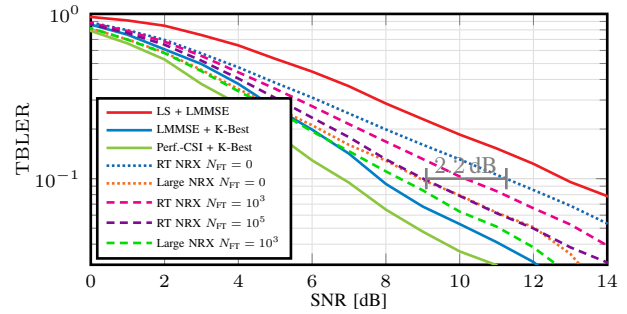


Fig. 7: TBLE vs. SNR with site-specific evaluation dataset in $U \times B \equiv 2 \times 4$ MU-MIMO with MCS index $i = 14$. Fine-tuned NRXs trained with $N_{TD} = 10^3$ samples.

with significant performance gains through site-specific fine-tuning, requiring only a few thousand iterations and data samples. We leaved fine-tuning on real-world measurement datasets as well as a system-level performance evaluation for future work.

REFERENCES

- [1] T. O’Shea and J. Hoydis, “An Introduction to Deep Learning for the Physical Layer,” *IEEE Trans. Cognitive Commun. Netw.*, vol. 3, no. 4, pp. 563–575, 2017.
- [2] M. Honkala, D. Korpi, and J. M. Huttunen, “DeepRx: Fully Convolutional Deep Learning Receiver,” *IEEE Trans. Wireless Commun.*, vol. 20, no. 6, pp. 3925–3940, 2021.
- [3] F. Ait Aoudia and J. Hoydis, “End-to-end learning for OFDM: From Neural Receivers to Pilotless Communication,” *IEEE Trans. Wirel. Commun.*, vol. 21, no. 2, pp. 1049–1063, 2021.
- [4] H. Ye, G. Y. Li, and B.-H. Juang, “Power of Deep Learning for Channel Estimation and Signal Detection in OFDM Systems,” *IEEE Wireless Commun. Lett.*, vol. 7, no. 1, pp. 114–117, 2017.
- [5] X. Lin, “Artificial Intelligence in 3GPP 5G-Advanced: A Survey,” *arXiv:2305.05092*, May 2023.
- [6] S. Cammerer, F. Ait Aoudia, J. Hoydis, A. Oeldemann, A. Roessler, T. Mayer, and A. Keller, “A Neural Receiver for 5G NR Multi-user MIMO,” in *Proc. IEEE Globecom Workshops*, Mar. 2023, pp. 329–334.
- [7] D. Korpi, M. Honkala, J. M. Huttunen, and V. Starck, “DeepRx MIMO: Convolutional MIMO Detection with Learned Multiplicative Transformations,” in *Proc. IEEE Int’l Conf. Commun. (ICC)*, Jun. 2021.
- [8] M. B. Fischer, S. Dörner, F. Krieg, S. Cammerer, and S. ten Brink, “Adaptive NN-based OFDM receivers: Computational complexity vs. achievable performance,” in *Proc. IEEE Conf. Rec. Asilomar Conf. Signals, Sys., and Comp.* IEEE, Oct. 2022, pp. 194–199.
- [9] N. Uzlaner, T. Raviv, N. Shlezinger, and K. Todros, “Asynchronous Online Adaptation via Modular Drift Detection for Deep Receivers,” *arXiv:2407.09134*, Jul. 2024.
- [10] J. Hoydis, F. Ait Aoudia, S. Cammerer, M. Nimier-David, N. Binder, G. Marcus, and A. Keller, “Sionna RT: Differentiable Ray Tracing for Radio Propagation Modeling,” in *Proc. IEEE Globecom Workshops*, Mar. 2023, pp. 317–321.
- [11] E. Dahlman, S. Parkvall, and J. Skold, *5G NR: The Next Generation Wireless Access Technology*. Academic Press, 2020.
- [12] ETSI, “ETSI TS 138 214 V16.2.0: Physical layer procedures for data,” Tech. Rep., Jul. 2020.
- [13] K. Pratik, B. D. Rao, and M. Welling, “RE-MIMO: Recurrent and Permutation Equivariant Neural MIMO Detection,” *IEEE Trans. Signal Process.*, vol. 69, pp. 459–473, 2021.
- [14] E. Nachmani, Y. Be’ery, and D. Burshtein, “Learning to Decode Linear Codes Using Deep Learning,” in *Proc. IEEE Ann. Allerton Conf. Commun., Contr., and Comput.*, Sep. 2016, pp. 341–346.
- [15] A. Gansekoele, A. Balatsoukas-Stimming, T. Brusse, M. Hoogendoorn, S. Bhulai, and R. van der Mei, “A Machine Learning Approach for Simultaneous Demapping of QAM and APSK Constellations,” *arXiv:2405.09909*, May 2024.
- [16] C. Studer and H. Bölcskei, “Soft-Input Soft-Output Single Tree-Search Sphere Decoding,” *IEEE Trans. Inf. Theory*, vol. 56, no. 10, pp. 4827–4842, Oct. 2010.